**Results in Materials**
**Volume 13, March 2022, 100264**

# Effects of powder compression and laser re-melting on the microstructure and mechanical properties of additively manufactured parts in laser-powder bed fusion

Muhannad Ahmed Obeidi[1,2,3*], Alex Conway[4], Andre Mussatto[1,2,3], Merve Nur Dogu[1,2,3], Sithara P. Sreenilayam[1,2,3], Hasan Ayub[1,2,3], Inam Ul Ahad [1,2,3], and Dermot Brabazon[1,2,3]

[1]I-Form Advanced Manufacturing Research Centre, Dublin City University, Dublin, Ireland
[2]School of Mechanical & Manufacturing Engineering, Dublin City University, Dublin, Ireland
[3]Advanced Processing Technology Research Centre, Dublin City University, Dublin, Ireland
[4]AMBER Research Centre, Science and Technology in Advanced Manufacturing Research Group (STAM), Trinity College Dublin, Ireland

*Corresponding author: muhannad.ahmedobeidi@dcu.ie

**Abstract:**

Achieving good surface profile and low levels of porosity are prime challenges in the Laser-Powder Bed Fusion (L-PBF) additive manufacturing technique. In order to optimise these properties, post-processing is often required. However, the compression of powder spread on the build plate and re-melting of each build layer during the L-PBF process could address these challenges. In this study, the effect of different powder compression ratios and laser re-melting regimes on the density, microstructure morphology, surface profile and mechanical properties of L-PBF produced parts were investigated. Two different metal printers with same laser processing parameters were used to fabricate 10 x 10 x 10 $mm^3$ stainless steel 316L samples. To examine the impact of compression ratio and layer re-melting, one set of samples was prepared with three different compression levels for each layer and a second set of samples either a single or double set of laser passes for each layer. The Volumetric Energy Density (VED) range examines was from 26.7 J/$mm^3$ to 80 J/$mm^3$. Density, hardness, elastic modulus, microstructure and surface profiles of the printed samples were characterised. A 3% increment in density and a 50% reduction in the surface roughness were achieved using a laser double pass over each layer. The results demonstrate, by applying different powder compression ratios onto the powder bed and by re-melting each layer, that the density, surface roughness and the elastic modulus of the produced samples can be improved.

**Keywords:** Laser powder bed fusion, Additive manufacturing, Powder compression, Laser re-melting, Nano-indentation, Archimedes density.

## 1. Introduction

In recent years, metal part production using the L-PBF process has advanced exponentially. The global AM market is estimated to reach 26.68 billion USD by 2027 [1] and L-PBF is the leading technology in the metal AM market [2]. This advanced AM technology uses a high energy source to melt powder in a metallic powder bed system. The process can be optimised such that parts have excellent mechanical properties by melting the metal powder at selected locations in the powder bed in a predefined manner according to the supplied CAD design file [3]–[10]. In the PBF process, data from a CAD model is sliced into thin layers at first and then each of the sliced layers are micro-welded one layer over the other. This process continues until the metal part according to the CAD file geometry is produced.



https://doi.org/10.1016/j.rinma.2022.100264

The L-PBF process is capable of manufacturing metal products from a variety of materials including, aluminium alloys (*e.g*., AlSi7Mg0.6, AlSi10Mg) [10], [11], nickel alloys (*e.g*., Haynes HX, Inconel 718, Inconel 625) [12]–[17], stainless steels (*e.g*., AISI 304, maraging steels, tool steels, AISI 3016L) [18], [19], cobalt alloys (*e.g*., CoCrMo) [20], magnesium alloy (*e.g*., WE43) [21]–[24], and titanium alloys (*e.g*., Ti6Al4V ELI, Ti6Al4V, CP-Titanium Grade 2) [25], [26]. The L-PBF process is a complicated manufacturing technique which involves large number of processing parameters that influence the final part properties. Processing parameters such as laser spot size, laser power, powder bed temperature, part position on the build plate with reference to powder deposition and inert gas inlet, initial particle size, scanning velocity, gas composition, gas flow rate, layer thickness and hatch spacing have different impacts on the physical and mechanical properties (*e.g*., strength, surface roughness, surface hardness, dimensional accuracy, wear resistance and colouring) of the developed final product. Obeidi et. al, [27] for example investigated the effect of the inert gas flow stream line on the spattered powder distribution on the build plate which have a high impact on the part quality and porosity. The researcher reported that an increase in the residual spattered powder can be found at the inert gas downstream region due to the gas effect as a carrier of the raising powder particles. For this reason, it was recommended to start scanning first those parts located near the inert gas outlet and then orderly progressing towards those ones near the inert gas inlet, while using an optimum inert gas flow rate. Mussatto et. al [28] investigated the influence of powder morphology on the formation of powder beds. They reported that particle segregation intensified as the powder particle size distribution increased and that the powder bed uniformity was maximised as particle spherisity and smoothness increased. Despite most commercial L-PBF printers use blade mechanisms to form powder beds because the particles experience significant less cohesive forces, roller mechanisms was reported to provide higher powder bed densities and uniformities . The choice of one mechanism over other is typically dictated by the powder particles physical and chemical properties and the powder bed characteristic requirements.

Nowadays, stainless steels are widely used due to their unique behaviours at high and room temperatures such as their good corrosion resistance, ductility and high strength [29]. Metal parts for critical high-tech industrial applications such as blades for jet engines, orthopaedic implants for bone replacement *etc*. can be developed using the PBF AM process. However, the level of confidence in the metal parts quality is a challenge that needs to be addressed for the more widespread use of this process in industry. During production, L-PBF AM processes are known to generate many material defects such as large lack-of-fusion defects [30], gas porosity [31] and keyhole porosity[32]. Numerous studies have already been reported on the formation, and reduction of these defects and mechanical properties of metal parts [33]–[39]. The continued fast heating and cooling of the metal micro-melt pools in the L-PBF process may lead to dimensional distortions and micro or macro-scale cracking resulting from process generated residual thermal stresses. Porosity in metal parts either as irregular shaped pores (keyholes) or uniform pores (spherical) is one of the key concerns in metal AM and it plays an important role in both crack initiation and propagation through the metal part [40], [41]. These porosities that form in various locations such as on or close to the metal parts surface, between adjacent deposited metal layers or within the individual metal layers, critically affect the produced metal part's mechanical strength, fatigue strength, corrosion resistance, fracture toughness and stiffness characteristics. The powder spread on the build plate manifests the fabrication process and the final part properties as it dictates the heat transfer and mass transfer during the material melting and solidification [42]–[44]. Uneven distribution or loosely spread



https://doi.org/10.1016/j.rinma.2022.100264

powder over the preceding layer could result in porosity, low mechanical properties and part geometry distortion [45]–[47]. In order to increase the packing density of powders, mixing of particles with different size distributions can be used to achieve higher density and low porosity in the L-PBF produced parts[47]–[49]. As mentioned above, a solution is to compress the powder bed to increase the packing density. For this, a rigid roller can be used to press the powder against the bed [50], [51]. Laser re-melting during the L-PBF is an in-process feasible remediating measure to tailor the microstructure and eliminate existing microstructural defects. It was show that re-melting by laser scanning the same layer twice can reduce porosity density and improve surface roughness, while reducing residual stresses . The residual stress within the metal parts due to the large thermal gradients present during the build leads to external and internal cracking and in the extreme condition it causes the delamination of individual deposited layers [52]. The quality of the final product strongly depends on the characteristics of the processing within each layer, including the powder distribution and the thermal filed resulting from the laser processing [28], [53], [54]. Hence, the understanding of metal powder compression and laser re-melting within the L-PBF technique is important for the industrial-scale manufacturing of highly precise and predefined metal parts with reproducible properties. This study therefore focuses on investigating the effects of metal powder compression and laser re-melting on the microstructure and mechanical properties of additively manufactured parts. Specifically, the density, hardness, elastic modulus, microstructure, and surface profiles of 316L L-PBF printed samples with different compression ratios and laser re-processing of each layer were characterised.

## 2. Experimental Conditions and Methods

### *2.1. Materials*

Gas atomised 316L stainless steel powder was used to produce the test samples. The metal powder was supplied by Carpenter Additive, UK, with same technical data that has been previously reported by Obeidi *et. al* [27]. The distribution and topography of powder spread on the machine bed and pouring characterization was as described in detail by Mussatto *et. al* [28]. Malvern Mastersizer 3000 was used to measure the powder particle size distribution. The powder particles geometry and sphericity was analysed by using scanning electron microscope (SEM) from Zeiss EVO LS-15. The chemical properties of the as supplied gas atomized 316L stainless steel (wt%) are given in Table 1.

**Table 1**: The chemical properties of the gas atomized 316 L stainless steel (wt%).

| C | Cr | Cu | Mn | Mo | Ni | N | O | P | Si | S | Fe |
|---|---|---|---|---|---|---|---|---|---|---|---|
| **0.03** | 17.6 | 0.02 | 0.66 | 2.38 | 12.5 | 0.09 | 0.03 | 0.007 | 0.65 | 0.006 | Bal. |

### *2.2. Experimental methods*

Two metal L-PBF printers, the Aconity*MINI* from Aconity GmbH and the ProX 200 from 3D Systems, were used to produce the test samples in this study. The metal printers are equipped with a 200 W fibre laser with 1068 nm wavelength. The build chamber was processed with argon gas atmosphere with oxygen levels of less than 20 ppm. Here a Design of Experiments (DoE) model of two factors at two levels was used to carry out the experimental work. The processing parameters for the DoE used in this study are listed in Table 2.



https://doi.org/10.1016/j.rinma.2022.100264

**Table 2** The implemented Design of Experiments process parameters and their levels

| Factor | Level-1 | Level-2 |
|---|---|---|
| Laser power (W) | 120 | 180 |
| Scanning speed (mm/s) | 500 | 1000 |

Other processing parameters were kept constants to help compare the results from the two printers. These parameters include the laser focal spot size of 70 µm, hatch spacing of 90 µm, layer thickness of 30 µm, a single contour around each layer with outer distance of 70 µm and a hatch starting angle of 0° with an angle rotation of 20 ° per layer in order to aid a reduction in level and isotropy of the resulting residual thermal stresses.

The powder spreading mechanism of the two metal printers is shown in Figure 1. In the case of Aconity*MINI*, Figure 1 (a), a slider blade transfers the metal powder from the powder supply and spreads it over the build plate. Different slider blades are available for use in this printer. A flexible rubber blade was used in this study, but the re-coater mechanism can also include rigid polymer or an anti-static carbon brush. In contrast, the mechanism used on the ProX 200 is composed of a rigid blade to spread the powder followed by a rigid material (hardened stainless-steel) roller to compress the powder layer in order to reduce the gaps between the powder particles, Figure 1 (b). The roller is fitted with a torque pre-loading to maintain a downward pressure versus the powder layer with a force safety sensor to avoid any damage caused by excessive loading, collision, or part's uplift.

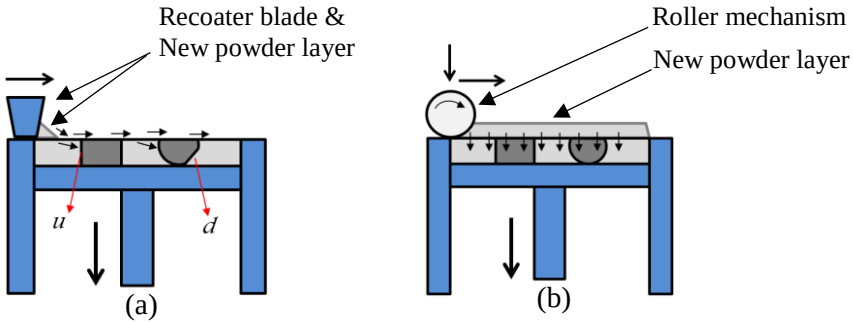


**Figure 1** The powder spreading mechanisms of the (a) Aconity*MINI* and (b) ProX 200 L-PBF machines.

For the production of test samples to investigate the impact of powder bed compression, the following experimental plan was carried out. Three different compression ratios (CR) were used to produce three sets of four 10×10×10 $mm^3$ cubes on the 3D Systems metal printer using the process parameters listed in Table . In order to achieve three different compression levels (termed as Compression Ratios ($C_x$) in this study) in the ProX 200 printer, the powder was spread multiple times for the set layer thickness while keeping the required layer thickness constant. For compression ratio 1 ($C_1$), the build plate was lowered by 30 µm which is equivalent to single layer thickness. The powder was spread across the build plate and compressed by the metal roller, as per the standard machine operation procedure. For compression ratio 2 ($C_2$), the build plate was lowered by 60 µm *(double the layer thickness)* and the powder was spread to fill the entire volume. The build plate was then lifted by 30 µm to keep the layer overall thickness same at 30 µm, and then was compressed by the metal roller. In this case, the excess powder is compressed into the 30 µm layer and creates the compression



https://doi.org/10.1016/j.rinma.2022.100264

ratio ($C_2$). Any excess powder is finally removed by the re-coater blade. For compression ratio 3 ($C_3$), the build plate was lowered by 90 µm and the powder was spread across the plate to fill the generated volume. The build plate was then lifted by 60 µm to keep the layer thickness constant at 30 µm. The increased quantity of excess powder was compressed into the 30 µm layer thickness using the metal roller, after which the excess powder was removed by the re-coater blade. In this way, three different compression ratios were achieved with one, two and three layers of extra powder compressed against the previous layer for compression ratios 1, 2, and 3 respectively. This strategy was repeated for all 334 layers to produce the 10 mm high cuboid samples with the three different compression ratios.

Separately, two sets of samples with a different number of laser layer processing scans were produced using the Aconity*MINI* printer. The same set of processing parameters listed in Table were used to produce these samples. One set was processed by melting each layer using a single laser pass while the second set was produced by laser processing each layer two times. In the latter case, the laser was scanned over each 2D layer according the same scan pattern.

### 2.3 The cross-sectional microstructure

The microstructure was revealed after polishing the produced samples by using grinding silicon carbide and diamond suspension from 240 µm down to 1 µm and for 3 to 5 minutes for each grit size. The grinding and polishing duty and the granular and crystallization microstructure was developed by chemically etching the polished samples with Adler etchant made up of 9 g copper ammonium chloride, 150 ml hydrochloric acid, 45 g hydrated ferric chloride, and 75 ml distilled water as reported previously by Obeidi *et al*. [53]. The micrographs shown in this study were obtained by using both Zeiss EVO LS-15 SEM and a 3D optical microscope from Keyence 2000.

### 2.4 The density

Archimedes principle was used to measure the density of the produced samples with three different fluids: acetone, ethanol and xylene.

### 2.5 The surface roughness and profile

A non-contact 3D optical microscope from Bruker Contour GT. The measured data gave full description of the surface profile and is reported in this paper by using the following three terms:

i. ($S_a$) expresses the mean of the absolute values of the surface departure above and below the mean plane within the sampling area.
ii. ($S_z$) expresses the average of the height difference between five highest peaks and the five lowest valleys
iii. ($R_a$) is the arithmetic mean of the absolute values of the roughness profile along a line.

### 2.6 The mechanical properties

Bruker HYSITRON TI Premier nano-indenter was used during this test. The characterisation was performed by using continuous stiffness measurement technique (CSM) with Berkovich diamond tip indenter. Prior to performing the test, the samples were mechanically polished by using silicon carbide paper up to 4000 grit followed by diamond suspension polisher of 3, 1, and 0.04 µm. A series of indents were applied in multiple replicates across the horizontal (x, y) plane and the vertical (Z) build direction with 0.1 mm spacing between the consecutive indents,



https://doi.org/10.1016/j.rinma.2022.100264

see Figure 2. During each indent, the loading and unloading rates were set to 2 mN/s until a maximum load (P) of 10 mN was reached and was held for 2 seconds dwell time. The equipment software was used to record the loading/unloading versus the displacement (depth) continuously and calculate the hardness as ($H = \frac{P_{max}}{\text{Indent area}}$), and the reduced elastic modulus (Er) which is a combined elastic modulus value of both the indenter and the specimen. The stiffness modulus of elasticity (S) was obtained from analysing the unloading plots.

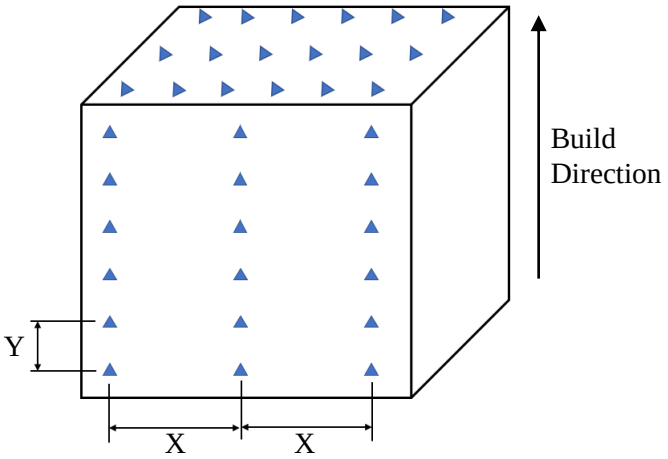


(a)

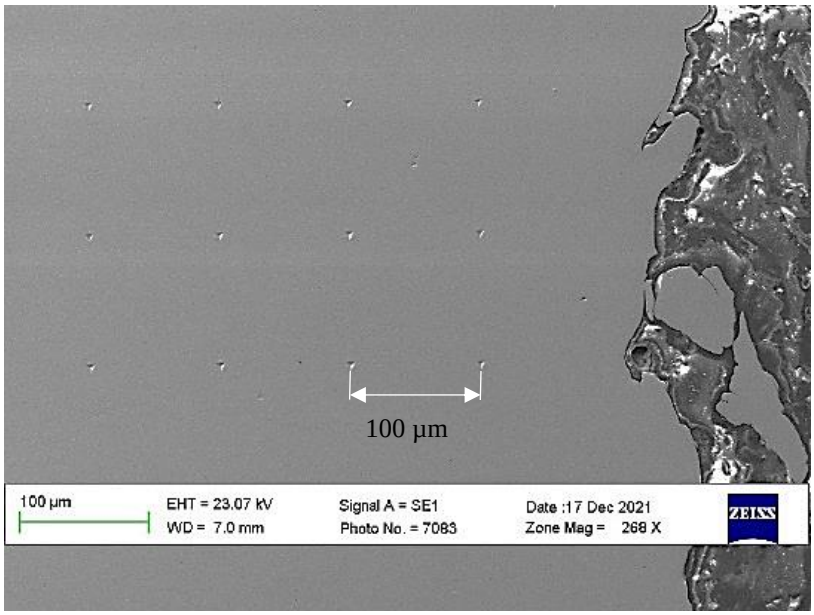


(b)

**Figure 2** (a) Schematic, and (b) SEM image showing the indentation spacings and lines



https://doi.org/10.1016/j.rinma.2022.100264

## 3. Results and Discussion

The SEM micrographs in Figure 3 show an acceptable powder particles sphericity and dispersity with almost no presence of satellite, agglomeration, or elongated particles. The powder particle size distribution (PSD) results showed $Dv_{10}$ =18 µm, $Dv_{50}$ = 30 µm and $Dv_{90}$ = 42.4 µm.

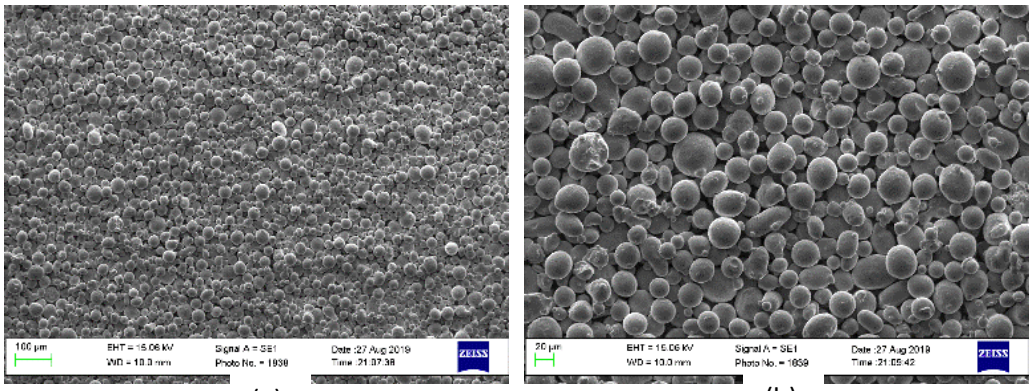


**Figure 3** SEM micrographs of the 316L SST powder used in this study at (a) low and (b) high magnification.

### 3.1 The measured density

Table 3 shows the sample processing parameters, volumetric thermal energy (VED) and the relative density measured by using Archimedes using ethanol as reference fluid. The VED was calculated as:

$$\text{VED}\ \left(\frac{J}{mm^3}\right) = \frac{\text{Laser beam power (W)}}{\text{Scanning speed}\left(\frac{\text{mm}}{\text{sec}}\right)\times\text{Hatch spacing (mm)}\times\text{Powder layer thickness (mm)}}$$

**Table 3** The input processing parameters and measured relative density (%) for the produced samples with the 95% confidence intervals, n = 4.

| S. No. | Laser power (W) | Scan speed (mm/sec) | VED J/mm$^3$ | Relative Density (%) measured by using Archimedes with ethanol | | | | |
|---|---|---|---|---|---|---|---|---|
| | | | | Aconity*MINI* | | ProX 200 | | |
| | | | | SP | DP | $C_1$ | $C_2$ | $C_3$ |
| 1 | 120 | 1000 | 26.7 | $89.76^{\pm0.3412}$ | $91.9^{\pm0.2527}$ | $89.79^{\pm1.38}$ | $90.02^{\pm2.39}$ | $92.43^{\pm2.11}$ |
| 2 | 180 | 1000 | 40.0 | $96.27^{\pm0.237}$ | $98.83^{\pm0.0678}$ | $95.54^{\pm0.04}$ | $95.08^{\pm0.33}$ | $95.45^{\pm0.14}$ |
| 3 | 120 | 500 | 53.3 | $96.51^{\pm0.244}$ | $99.75^{\pm0.0785}$ | $97.33^{\pm0.87}$ | $97.62^{\pm0.93}$ | $98.22^{\pm1.09}$ |
| 4 | 180 | 500 | 80.0 | $96.72^{\pm0.2023}$ | $98.68^{\pm0.0515}$ | $97.58^{\pm0.09}$ | $97.43^{\pm0.05}$ | $98.83^{\pm0.08}$ |

The density results obtained showed improvement in the measured density for the samples re-melted by the laser beam (double pass, DP) compared with those melted with a single laser pass (SP) on the Aconity*MINI* printer. Sample 1 produced with the lowest VED of 26.7 J/mm$^3$ showed the lowest relative density (89.76%) among the produced samples scanned with just one laser pass. This result can be explained by the low VED applied due to the low laser power



https://doi.org/10.1016/j.rinma.2022.100264

and high scanning speed which in turn resulted in a lack of fusion. When the same processing parameters were applied with laser re-melting (DP) of the powder layers, the relative density was increased to 91.9%. In contrast, cube sample 2 which was processed with a higher VED exhibited enhanced density which can be explained by the increased extent of melting of the powder. A minor enhancement in some of the samples densities produced by increasing the powder compression ratio ($C_x$) is indicated from the results. Since AM is a thermal process, this limited increase in the density can be explained by the actual amount of thermal energy applied and the exact energy needed for the full melting of the metal powder after compression. The powder layer thickness is equal to the average particle size $D_{V50}$ of 30 microns. The larger particles are removed by the re-coater blade while the smaller particles are forced to fill the gaps. This will results in (*i*) more material deposition despite the fixed layer thickness, and (*ii*) increase in the thermal conductivity of the molten layer which leads to a greater heat dissipation to the previously solidified layers. Both results indicate more thermal energy is required to reach the full melting conditions and also to be compared with the results obtained from the Aconity and the lower ($C_x$) ratios samples. In this study, the same energy levels were employed for each sample (Table 3) to facilitate the direct comparison of the measured mass values and to identify the correlation between these values and the powder compression.

It can be seen that for the processing conditions used, there were differences between the relative densities measured on the samples produced from the two printers with the single pass produced samples from the Aconity being of marginally lower density and the double pass resulting in a higher density. It is important to note that the process parameters should be optimised for each machine before making conclusions about machine capability [18], [27].

Figure 4 shows the density plots measured by Archimedes principle with ethanol. The cubes printed on the Aconity*MINI* showed a noticeable increased density in the laser re-melted (double pass, DP) cubes compared to those processed with a single pass (SP). Also, a larger grain size was observed in the (DP) cubes caused by the re-melting in a process similar to annealing in which the cooling rates were interrupted and slowed down by the second laser beam irradiation, see Figure 10.

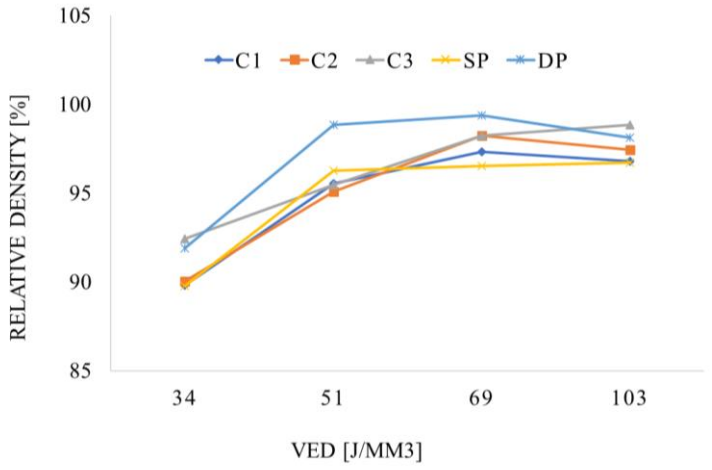


**Figure 4** The average relative densities measured by Archimedes with ethanol (95% CI error bars are smaller than the point markers)



https://doi.org/10.1016/j.rinma.2022.100264

Using the Archimedes method, close density values and plot trends were obtained for the different fluids used in this study. Comparing the Archimedes test results using the three suspension fluids, it was observed that xylene resulted in lower densities of the measured samples compared to using either acetone or ethanol. The density measurements were taken with three repetitions for each sample. The confidence interval at 95% was quite large in the case of xylene for all samples compared using to acetone and ethanol. Here the density of the suspension liquid plays important role. Xylene (861 kg/m3) density is higher comparing to ethanol (789 kg/m3) and acetone (784 kg/m3). Therefore, xylene produced increased buoyancy and thus higher margins of errors were recorded. Since acetone and ethanol have similar densities, the density results obtained using these suspension liquids were similar and had a tighter confidence interval. Nevertheless, density results obtained for the samples using all three suspension liquids followed a similar pattern with respect to the sample change in VED provided during sample fabrication. Therefore, only the density results obtained using ethanol are presented here because of their high repeatability and stable measurement.

From Archimedes results, it was observed that the measured density increases with the increase in the VED. This correlation can be explained by the sufficient melting provided with the higher VED values which was also reported in the literature [56]–[58]. This concept of relative density increase for samples processed with higher VED, is similar to previously reported results by Nguyen *et al.* on stainless steel 304L samples using gas pycnometer and a single laser pass [57]. It is interesting to note that in the current study, without extensive parameter optimisation, a 96% relative density was achieved using single pass laser. A noticeable increase in the (DP) cubes density versus the (SP). Also, no significant improvement in the parts' densities with the increase of the powder compression ratios between $C_1$ and $C_2$ was observed, and only a limited increase was noted in the case of $C_3$, see Figure 4 (b). The reduction of densities which was noted on some samples in this figure at the high VED levels (right hand side of the plot) can be explained by the over-melting and the formation of keyholes, see Figure 5. In this figure, the samples processed with laser beam double-pass in three different VED were grinded and polished in the (x, y) plane perpendicular to the build direction near the top build layers. The SEM figures show the un-melted powder particles trapped in large pores due to the lack of melting in the low VED level, Figure 5 (a). A significant enhancement in the sample topology and density when processed with 53.3 J/mm$^3$ while a presence of keyholes was noted at the higher VED level of 80 J/mm$^3$ due to over-melting and gas trapping, Figure 5 (b) and (c).

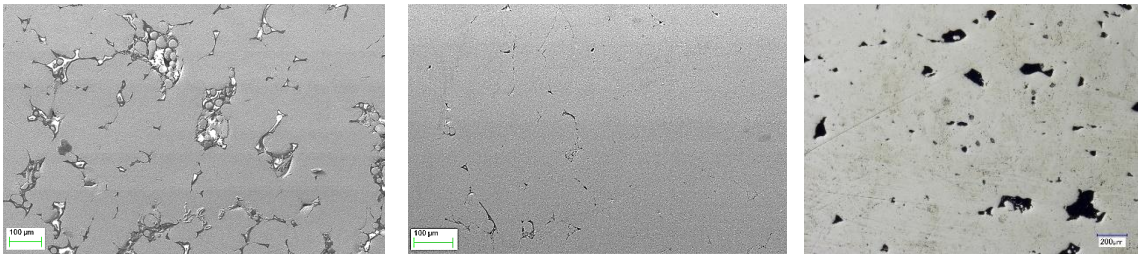

(a) (b) (c)

**Figure 5** SEM micrographs of the internal porosity formed in the horizontal plane of the double-pass samples for VEDs of (a) 26.7, (b) 53.3, and (c) 80 J/mm$^3$.



https://doi.org/10.1016/j.rinma.2022.100264

### 3.2 The surface profile

The different mechanisms used during the metal powder deposition and the increase in the powder compression ratio had noticeable effects on the surface profile and topography, see Figure 6 and Table 4. The data presented in Table 4 noted the clear improvement in the surface roughness for double pass (DP) compared with single pass (SP) processing. Sample 1 processed with (120 W and 1000 mm/sec) showed a large improvement in the surface roughness after the second laser pass.

**Table 4** Surface profile parameter values obtained for Sample 1processing conditions.

| Profile Property | Aconity*MINI* | | ProX 200 | | |
|---|---|---|---|---|---|
| | Single pass (SP) | Double pass (DP) | Compression Ratio 1 ($C_1$) | Compression Ratio 2 ($C_2$) | Compression Ratio 3 ($C_3$) |
| Arithmetical Mean Height $S_a$ (µm) | 27.84 | 13.81 | 33.45 | 33.6 | 35.21 |
| Maximum Height $S_z$ (µm) | 343.87 | 305 | 350 | 374.66 | 379.11 |
| Average Surface Roughness $R_a$ (µm) | 29.23 | 14.67 | 23.51 | 24.64 | 27.03 |

A significant increase in the surface roughness values was observed for all the samples produced on the ProX 200 compared to those from the Aconity*MINI* as shown in Figure 6. The high ($S_a$) values obtained in the ($C_3$) scenario can be explained by the creation of mechanical bonding between the powder particles in the consecutive layers. This type of mechanisms results in more partially melted and sintered powder particles formed with line marks as can be seen in Figure 6 (right). The modified surface profile exhibited by the samples produced with ($C_3$) might affect the final application of the part. Applications like biomedical and aerospace require high surfaces quality and reduced friction and may require post processing to reduce the surface roughness and waving. Figure 7 shows the 3D surface profile images for L-PBF produced samples obtained with the Bruker Contour GT optical microscope.

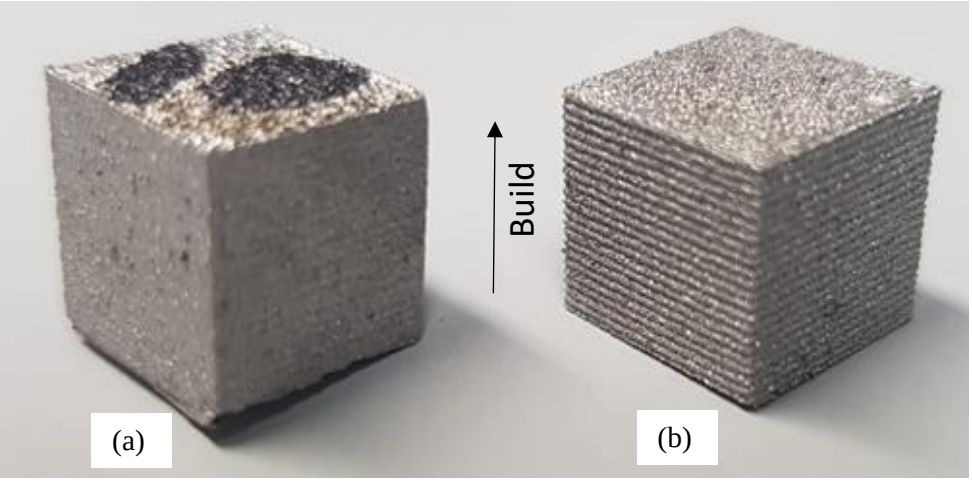


**Figure 6** Optical image of cubes produced according to sample 1 processing conditions, produced on the (a) Aconity*MINI* (DP) and (b) ProX 200 with $C_3$.



https://doi.org/10.1016/j.rinma.2022.100264

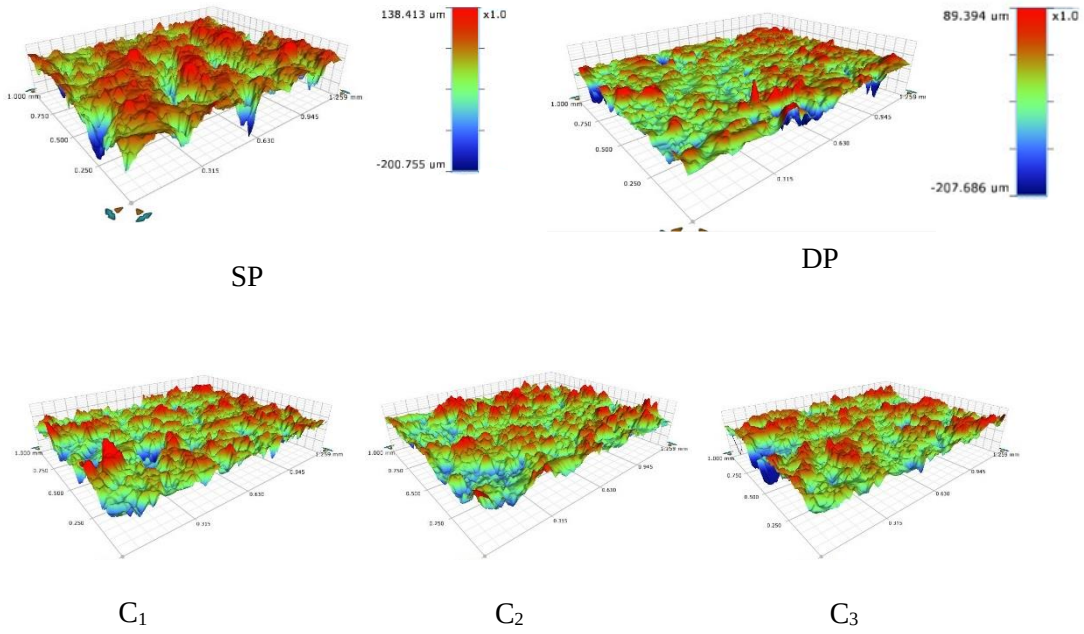


**Figure 7** Surface profile and topography for the single and double pass laser scan samples and the samples produced using the different compression ratios $C_1$, $C_2$ and $C_3$

The improved surface roughness in the case of DP sample was achieved due to the re-melting during the L-PBF process similar to the laser polishing process [1], [41], [59]. This also explains the significant reduction in the absolute distance between the maximum peak and minimum valley heights ($S_z$).

These differences in the AM part surface topographies and their importance for some applications were investigated and assessed by several researchers. For example, Obeidi *et al*. [1] and El Hassanin *et al*. [60] explored the surface characteristics of 316L stainless steel and AlSi10Mg parts produced by L-PBF and achieved an 80% enhancement of the surface roughness after post processing by laser beam polishing.

Another important comparison between the types of powder deposition systems, is that linear blade re-coater, Figure 1 (a) transfers and feeds the metal powder horizontally. Due to this horizontal transport, the metal powder particles experience two different scenarios, the upstream (*u*) and the downstream (*d*). In the upstream scenario, a sufficient build up and sustainability of powder occurs as the powder feed collides with the front edge of the build part. As opposed to that, and depending on the part geometry, the edge effect on the downstream side (*d*) can exhibit a separation line and a relative lack of metal powder supplied as the re-coater blade travels. This effect will increase if the powder particles have satellites with irregular and elongated geometry [30]. Moreover, the AM part design geometry and orientation with reference to the powder deposition direction can negatively contribute in the lack of powder feeding and distribution. Figure 8 shows 9 mm cylinders produced by using the linear re-coater mechanism during the preparation and setting-up of this study and in order to have a better understanding of the part orientation and geometry to be adopted.



https://doi.org/10.1016/j.rinma.2022.100264

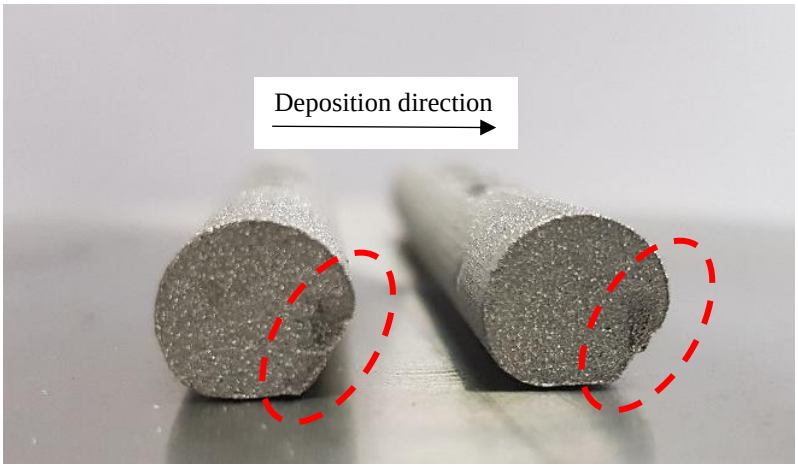


**Figure 8** 316L cylinders printed with deformation on the downstream side due to the lack of metal powder deposition.

This defect can be reduced or avoided mainly by re-orienting the part along the powder deposition direction, optimizing the powder particle size and geometry, optimizing the powder supply factor, optimizing the feed rates, and applying supporting structures. This type of defect was not observed in the roller re-coater mechanism as the roller compresses the powder in the vertical direction which could compensates for and fill any gaps in the powder bed density.

### 3.3 Microstructure

No significant evidence was found for the effect of the alteration in the powder compression on the grain size. Taking in account the difference in the scale bar, Figure 9 (a) and (b) shows SEM images of the cross-sectional view in the build direction, for sample 4 processing conditions at $C_1$ and $C_3$ as an example.

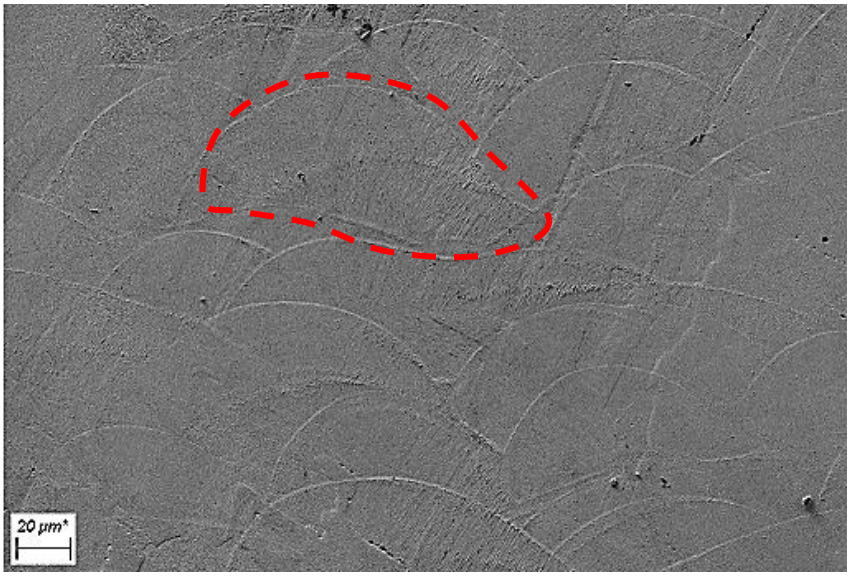


(a)



https://doi.org/10.1016/j.rinma.2022.100264

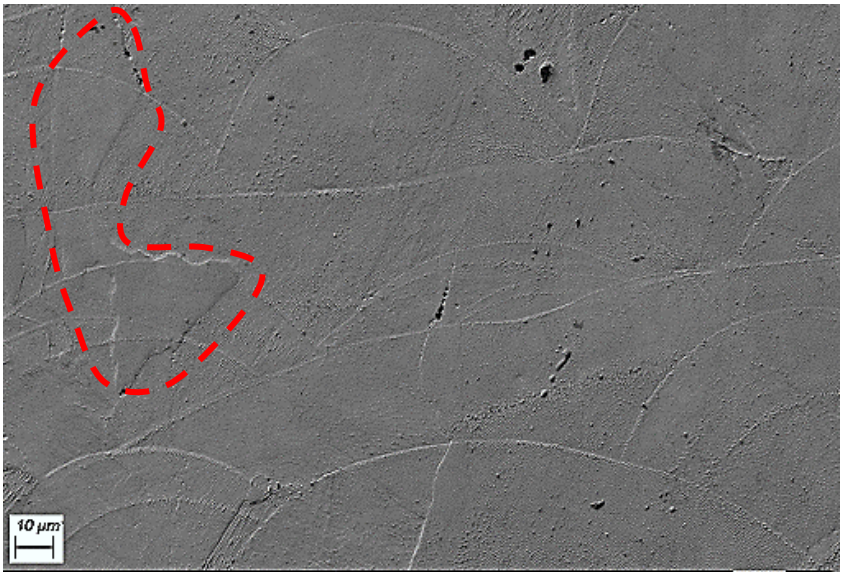


(b)

**Figure 9** SEM micrographs of sample 2 processing conditions produced samples on ProX200 using compression ratios of (a) $C_1$ and (b) $C_3$.

A clear effect of the laser re-melting was noted on both the build layer boundaries and the grain size. The re-melting of the solidified layer while still at high elevated temperature allows for sufficient time of cooling and a significantly decrease in cooling rates. Figure 10 shows optical images of the cross-sectional view of sample 2, processing condition produced samples on the Aconity*MINI* by (a) single pass and (b) double pass, in the build (z) direction.

It can be clearly seen that build layer boundaries were significantly removed after the re-melting and that the successive layers were merged together. This alteration enhanced the density and would be considered to enhance also the mechanical properties such as strength and ductility due in addition to the improved density, also due to the improved chemical bonding. A larger grain and melt-pool size were observed in the re-melted (DP) samples.

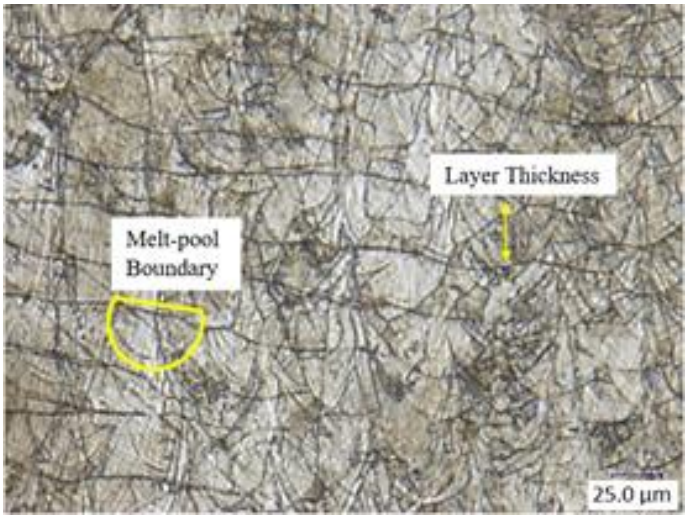


(a)



https://doi.org/10.1016/j.rinma.2022.100264

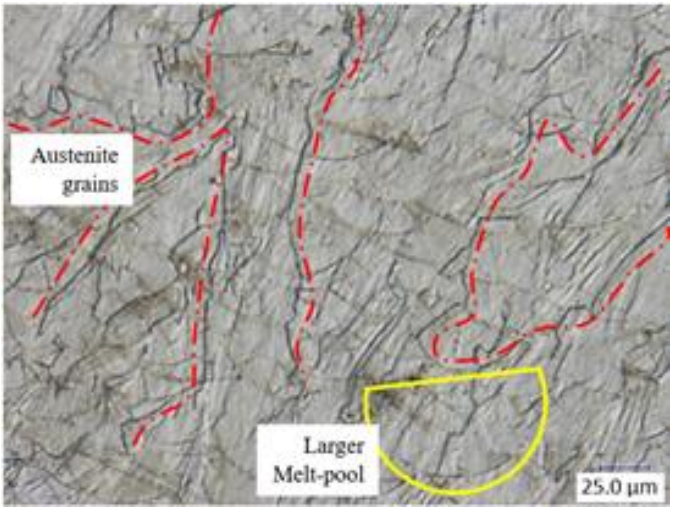


(b)

**Figure 10** Optical images of the cross-sectional view of sample 2 processing conditions for a (a) SP and (b) DP laser scan.

### 3.4 The mechanical properties (Nano-indentation)

The measured hardness results showed a lot of variability while a significant effect of the processing conditions on the reduced elastic modulus was recorded, see Figure 11 (a). The hardness data exhibit a broad distribution ranging between 3.2 and 4.5 GPa. The samples produced on the Aconity*MINI* showed reduced hardness when double scanned by the laser beam (DP) and a significant reduction in reduced elastic modulus. This reduction resulted from the additional heat energy applied by the second scan in a process, causing localised material annealing. This is noted from the larger melt-pool size in addition to the significant merging of the consecutive build layers as shown in Figure 10 (b). This could also explain the reduction in the stiffness elastic modulus (S) for sample (DP) as a result of the larger grain size and its associated effect on increasing the ductility.

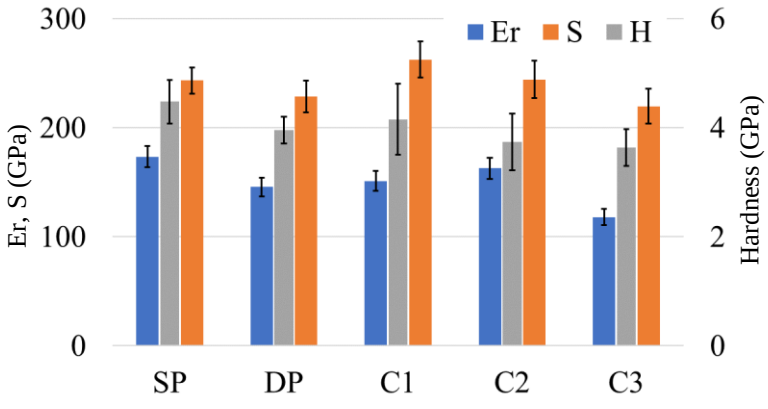


(a)



https://doi.org/10.1016/j.rinma.2022.100264

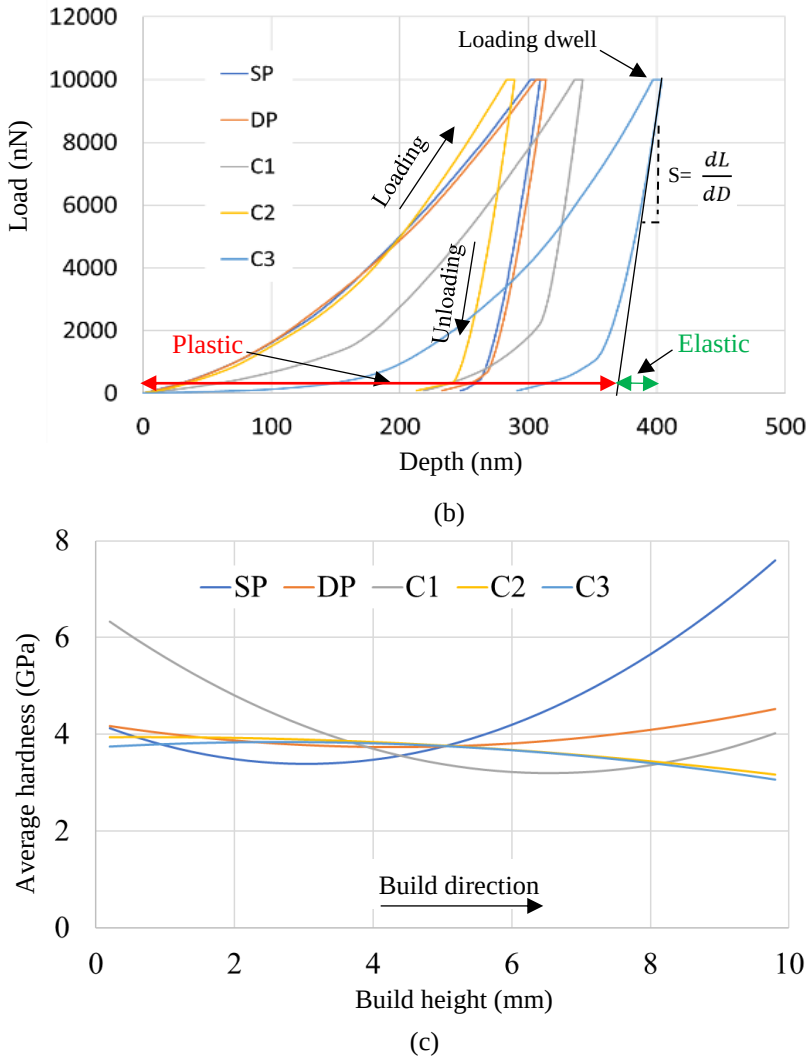


**Figure 11** Nano-indentation test results in the (Z) build direction, (a) the reduced elastic modulus (Er), elastic stiffness (S) and Hardness (H), (b) the loading/unloading plots, and (c) the average hardness (H) versus build height corresponding to Figure 2.

From Figure 11 (a), it can be noted that the hardness is proportional to the elastic modulus (S). The latter term is calculated from the slope of the unloading plot as: S=(dL/*dD*). Due to the higher energy density and lower rate of cooling, samples (DP) and ($C_3$) exhibit lower (S) values and thus the larger elastic deformation, Figure 11 (b). Oppositely, sample ($C_1$) with the low compression ratio, showed higher stiffness and thus the lower elasticity and elongation. This could be attributed to both the higher level of porosity (lower density) as shown in Figure 4.

Figure 11 (c) shows the average hardness evolution through the build layers of the five produced samples. The samples processed by a single pass (SP) exhibit relative reduction in the average hardness in the first couple of millimetres (early layers) in a similar scenario to that present in samples (DP) and ($C_1$). This could be caused by the resulting increase in solidified metal temperature while the resolidified mass is still small and there is not a sufficient volume of material for the heat transfer which therefore results in grain growth as the number of early layers increase. In the later layers where there is more solid material and surface area available for the heat dissipation, where higher cooling rates result in smaller grain size and an increased hardness. Samples $C_2$ and $C_3$ showed a stable level of hardness through the entire build layers.



https://doi.org/10.1016/j.rinma.2022.100264

This could potentially be due to their improved density and the elimination of the gaps between the powder particles which would otherwise act as heat transfer barriers.

## 4. Conclusion

In this study, the influence of the metal powder compression and the laser re-melting of 316L stainless steel parts during a laser powder bed fusion process on two machines were investigated. Using the same processing parameters, cuboid samples were produced on the Aconity*MINI* and 3D Systems ProX200 laser powder bed fusion systems. It was demonstrated that a density enhancement of up to 3% can be achieved by increasing the powder compression ratio from 1 to 3 times depending on the volumetric energy applied. This resulted in a reduction in the elastic modulus of 17%, from 262 to 219 GPa. Considering the simple cuboid geometry investigated in this study, these results could have greater significance in the case of complex geometries where consistent powder spreading may be more difficult. Higher improvement in the parts density is expected to be resulted by the readjusting the input volumetric energy density with accordance to the powder compression ration but this is out the focus of the current study.

A wide range of the volumetric energy density (VED) was applied, between 26.7 to 80 J/mm$^3$. Within this rage, a strong direct proportion correlation was observed between the AM part's density and the VED of processing. The re-melted layers of the samples processed by laser double pass showed an increase in density over those process just with one pass. A reduction in the density from 99.35 to 98.12% was overserved when the VED was increased from 69 to 80 J/mm$^3$ which could be associated to over-melting and related keyhole porosity formation. Laser dual pass processing of the build layers was shown to on average, within the investigated range, improve the surface roughness by 50% and the AM part density by 3%.

## Acknowledgments

This publication has emanated from research supported by a research grant from Science Foundation Ireland (SFI) under grant number 16/RC/3872 and is co-funded under the European Regional Development Fund. Parts and samples for this project were manufactured using facilities in the Additive Research Laboratory at the AMBER centre, CRANN Institute, Trinity College Dublin, Ireland. The AR-Lab is an SFI supported research centre.



https://doi.org/10.1016/j.rinma.2022.100264

## References

[1] "Additive Manufacturing Market to Reach USD 26.68 Billion By 2027 | CAGR of 14.4%: Reports and Data." https://www.prnewswire.com/news-releases/additive-manufacturing-market-to-reach-usd-26-68-billion-by-2027--cagr-of-14-4-reports-and-data-301163846.html (accessed Jun. 24, 2021).

[2] "Metal Additive Manufacturing market valued at EUR 2.02 billion in 2019," *AM Power Report*, 2019. https://additive-manufacturing-report.com/additive-manufacturing-market (accessed Jun. 24, 2021).

[3] V. Mahato, M. A. Obeidi, D. Brabazon, and P. Cunningham, "Detecting voids in 3D printing using melt pool time series data," *J. Intell. Manuf.*, pp. 1–8, Oct. 2020, doi: 10.1007/s10845-020-01694-8.

[4] N. Guo and M. C. Leu, "Additive manufacturing: Technology, applications and research needs," *Frontiers of Mechanical Engineering*, vol. 8, no. 3. Springer, pp. 215–243, Sep. 08, 2013, doi: 10.1007/s11465-013-0248-8.

[5] J. P. Kruth, G. Levy, F. Klocke, and T. H. C. Childs, "Consolidation phenomena in laser and powder-bed based layered manufacturing," *CIRP Ann. - Manuf. Technol.*, vol. 56, no. 2, pp. 730–759, Jan. 2007, doi: 10.1016/j.cirp.2007.10.004.

[6] L. Fitzsimons, G. McNamara, M. Obeidi, and D. Brabazon, "The Circular Economy: Additive Manufacturing and Impacts for Materials Processing," in Encyclopedia of Renewable and Sustainable Materials, Elsevier, 2020, pp. 81–92.

[7] J. P. Kruth, "Material Incress Manufacturing by Rapid Prototyping Techniques," *CIRP Ann. - Manuf. Technol.*, vol. 40, no. 2, pp. 603–614, Jan. 1991, doi: 10.1016/S0007-8506(07)61136-6.

[8] M. A. Obeidi, M. Monu, C. Hughes, D. Bourke, M. N. Dogu, J. Francis, M. Zhang, I. Ul Ahad, D. Brabazon, "Laser beam powder bed fusion of nitinol shape memory alloy (SMA)", Journal of Materials Research and Technology, 14, 2021, 2554-2570

[9] H. Sohrabpoor *et al.*, "Experimental and empirical model analysis of microsurface texturing on 316 L press-fit joints fabricated by selective laser melting," *Int. J. Adv. Manuf. Technol.*, vol. 108, no. 9–10, pp. 2687–2699, Jun. 2020, doi: 10.1007/s00170-020-05458-9.

[10] L. Tonelli, E. Liverani, A. Morri, and L. Ceschini, "Role of Direct Aging and Solution Treatment on Hardness, Microstructure and Residual Stress of the A357 (AlSi7Mg0.6) Alloy Produced by Powder Bed Fusion," *Metall. Mater. Trans. B*, May 2021, doi: 10.1007/s11663-021-02179-6.

[11] Q. Yang, C. Xia, Y. Deng, X. Li, and H. Wang, "materials Microstructure and Mechanical Properties of AlSi7Mg0.6 Aluminum Alloy Fabricated by Wire and Arc Additive Manufacturing Based on Cold Metal Transfer (WAAM-CMT)," *mdpi.com*, vol. 12, no. 16, Aug. 2019, doi: 10.3390/ma12162525.

[12] M. A. Obeidi, E. McCarthy, B. O'Connell, I. U. Ahad, and D. Brabazon, "Laser polishing of additive manufactured 316L stainless steel synthesized by selective laser melting," Materials (Basel)., vol. 12, no. 6, p. 991, Mar. 2019, doi:



https://doi.org/10.1016/j.rinma.2022.100264

10.3390/ma12060991.

[13] Y. Tang *et al.*, "Corrosion Behavior of a Selective Laser Melted Inconel 718 Alloy in a 3.5 wt.% NaCl Solution," *J. Mater. Eng. Perform.*, May 2021, doi: 10.1007/s11665-021-05909-8.

[14] N. Jeyaprakash, C. H. Yang, and K. R. Ramkumar, "Microstructural, mechanical and wear behaviour of Inconel-718 produced through laser-powder bed-fused additive manufacturing," *Mater. Sci. Technol. (United Kingdom)*, vol. 37, no. 3, pp. 326–337, 2021, doi: 10.1080/02670836.2021.1893457.

[15] Y. Tang *et al.*, "Corrosion Behavior of a Selective Laser Melted Inconel 718 Alloy in a 3.5 wt.% NaCl Solution," *Springer*, Accessed: Jun. 24, 2021. [Online]. Available: https://link.springer.com/article/10.1007/s11665-021-05909-8.

[16] G. Marchese *et al.*, "Microstructural evolution of post-processed Hastelloy X alloy fabricated by laser powder bed fusion," *Materials (Basel).*, vol. 12, no. 3, 2019, doi: 10.3390/ma12030486.

[17] C. Mandolfino, M. Obeidi, E. Lertora, and D. Brabazon, "Comparing the adhesion strength of 316L stainless steel joints after laser surface texturing by CO2 and fiber lasers," *Int. J. Adv. Manuf. Technol.*, vol. 109, no. 3–4, pp. 1059–1069, Jul. 2020, doi: 10.1007/s00170-020-05639-6.

[18] M. A. Obeidi *et al.*, "Comparison of the porosity and mechanical performance of 316L stainless steel manufactured on different laser powder bed fusion metal additive manufacturing machines," *J. Mater. Res. Technol.*, Jun. 2021, doi: 10.1016/j.jmrt.2021.06.027.

[19] C. Zitelli, P. Folgarait, and A. Di Schino, "Laser powder bed fusion of stainless steel grades: A review," *Metals*, vol. 9, no. 7. MDPI AG, p. 731, Jul. 01, 2019, doi: 10.3390/met9070731.

[20] H. Li, M. Wang, D. Lou, W. Xia, and X. Fang, "Microstructural features of biomedical cobalt–chromium–molybdenum (CoCrMo) alloy from powder bed fusion to aging heat treatment," *J. Mater. Sci. Technol.*, vol. 45, pp. 146–156, 2020, doi: 10.1016/j.jmst.2019.11.031.

[21] M. Esmaily *et al.*, "A detailed microstructural and corrosion analysis of magnesium alloy WE43 manufactured by selective laser melting," *Addit. Manuf.*, vol. 35, 2020, doi: 10.1016/j.addma.2020.101321.

[22] Saprykin, Y. P. Sharkeev, N. Saprykina, and E. A. Ibragimov, "Selective laser melting of magnesium," in *Key Engineering Materials*, 2020, vol. 839 KEM, pp. 144–149, doi: 10.4028/www.scientific.net/KEM.839.144.

[23] S. Gangireddy, B. Gwalani, K. Liu, E. J. Faierson, and R. S. Mishra, "Microstructure and mechanical behavior of an additive manufactured (AM) WE43-Mg alloy," *Addit. Manuf.*, vol. 26, pp. 53–64, 2019, doi: 10.1016/j.addma.2018.12.015.

[24] W. Frank, J. Lucas, M. Wolfgang, K. Zienab, S. Kristin, and S. Tanja, "Open-porous biodegradable magnesium scaffolds produced by selective laser melting for individualized bone replacement.," *Front. Bioeng. Biotechnol.*, vol. 4, 2016, doi:



https://doi.org/10.1016/j.rinma.2022.100264

10.3389/conf.fbioe.2016.01.00708.

[25] T. Grover *et al.*, "Role of titanium in bio implants and additive manufacturing: An overview," in *Materials Today: Proceedings*, 2019, vol. 26, pp. 3071–3080, doi: 10.1016/j.matpr.2020.02.636.

[26] H. Attar, S. Ehtemam-Haghighi, N. Soro, D. Kent, and M. S. Dargusch, "Additive manufacturing of low-cost porous titanium-based composites for biomedical applications: Advantages, challenges and opinion for future development," *J. Alloys Compd.*, vol. 827, 2020, doi: 10.1016/j.jallcom.2020.154263.

[27] M. Ahmed Obeidi et al., "Comprehensive assessment of spatter material generated during selective laser melting of stainless steel," Mater. Today Commun., vol. 25, p. 101294, Dec. 2020, doi: 10.1016/j.mtcomm.2020.101294.

[28] A. Mussatto, R. Groarke, A. O'Neill, M. A. Obeidi, Y. Delaure, and D. Brabazon, "Influences of powder morphology and spreading parameters on the powder bed topography uniformity in powder bed fusion metal additive manufacturing," Addit. Manuf., vol. 38, p. 101807, Feb. 2021, doi: 10.1016/j.addma.2020.101807.

[29] W. E. Luecke and J. A. Slotwinski, "Mechanical properties of austenitic stainless steel made by additive manufacturing," *J. Res. Natl. Inst. Stand. Technol.*, vol. 119, pp. 398–418, 2014, doi: 10.6028/jres.119.015.

[30] K. Darvish, Z. W. Chen, and T. Pasang, "Reducing lack of fusion during selective laser melting of CoCrMo alloy: Effect of laser power on geometrical features of tracks," *Mater. Des.*, vol. 112, pp. 357–366, 2016, doi: 10.1016/j.matdes.2016.09.086.

[31] W. E. King *et al.*, "Observation of keyhole-mode laser melting in laser powder-bed fusion additive manufacturing," *J. Mater. Process. Technol.*, vol. 214, no. 12, pp. 2915–2925, 2014, doi: 10.1016/j.jmatprotec.2014.06.005.

[32] B. Zhang, Y. Li, and Q. Bai, "Defect Formation Mechanisms in Selective Laser Melting: A Review," *Chinese Journal of Mechanical Engineering (English Edition)*, vol. 30, no. 3. pp. 515–527, 2017, doi: 10.1007/s10033-017-0121-5.

[33] T. H. Hsu *et al.*, "Effect of processing parameters on the fractions of martensite in 17-4 PH stainless steel fabricated by selective laser melting," *J. Alloys Compd.*, vol. 859, 2021, doi: 10.1016/j.jallcom.2020.157758.

[34] R. E. Napolitano, S. Jain, C. Sobczak, B. A. Augustine, and E. M. Johnson, "Build Optimization for Selective Laser Melting of 316L Stainless Steel and Parameterization for Cross-Material Comparison and Process Design," J. Mater. Eng. Perform., May 2021, doi: 10.1007/s11665-021-05861-7.

[35] P. Gao et al., "Effect of heat treatment on microstructure and mechanical properties of Fe–Cr–Ni–Co–Mo maraging stainless steel produced by selective laser melting," Mater. Sci. Eng. A, vol. 814, 2021, doi: 10.1016/j.msea.2021.141149.

[36] D. Dong et al., "Selective laser melting (SLM) of CX stainless steel: Theoretical calculation, process optimization and strengthening mechanism," J. Mater. Sci. Technol., vol. 73, pp. 151–164, 2021, doi: 10.1016/j.jmst.2020.09.031.



https://doi.org/10.1016/j.rinma.2022.100264

[37] G. O. Barrionuevo, J. A. Ramos-Grez, M. Walczak, and C. A. Betancourt, "Comparative evaluation of supervised machine learning algorithms in the prediction of the relative density of 316L stainless steel fabricated by selective laser melting," Int. J. Adv. Manuf. Technol., vol. 113, no. 1–2, pp. 419–433, Mar. 2021, doi: 10.1007/s00170-021-06596-4.

[38] G. Sander, A. P. Babu, X. Gao, D. Jiang, and N. Birbilis, "On the effect of build orientation and residual stress on the corrosion of 316L stainless steel prepared by selective laser melting," Corros. Sci., vol. 179, 2021, doi: 10.1016/j.corsci.2020.109149.

[39] X. Yang et al., "Subgrain microstructures and tensile properties of 316L stainless steel manufactured by selective laser melting," J. Iron Steel Res. Int., Mar. 2021, doi: 10.1007/s42243-021-00561-x.

[40] W. Yu, S. L. Sing, C. K. Chua, and X. Tian, "Influence of re-melting on surface roughness and porosity of AlSi10Mg parts fabricated by selective laser melting," J. Alloys Compd., vol. 792, pp. 574–581, Jul. 2019, doi: 10.1016/j.jallcom.2019.04.017.

[41] M. A. Obeidi, E. McCarthy, I. Ul Ahad, and D. Brabazon, "Improving the Surface Finish and other Properties of Engineering Metal Parts," Key Eng. Mater., vol. 813, pp. 197–202, Jul. 2019, doi: 10.4028/www.scientific.net/kem.813.197.

[42] R. Li, J. Liu, Y. Shi, L. Wang, and W. Jiang, "Balling behavior of stainless steel and nickel powder during selective laser melting process," Int. J. Adv. Manuf. Technol., vol. 59, no. 9–12, pp. 1025–1035, Apr. 2012, doi: 10.1007/s00170-011-3566-1.

[43] R. McCann *et al.*, "In-situ sensing, process monitoring and machine control in Laser Powder Bed Fusion: A review," *Addit. Manuf.*, vol. 45, p. 102058, Sep. 2021, doi: 10.1016/j.addma.2021.102058.

[44] A. Mussatto *et al.*, "Evaluation via powder metallurgy of nano-reinforced iron powders developed for selective laser melting applications," *Mater. Des.*, vol. 182, 2019, doi: 10.1016/j.matdes.2019.108046.

[45] ISO/ASTM, "Additive Manufacturing - General Principles Terminology (ASTM52900)," *Rapid Manuf. Assoc.*, pp. 10–12, 2013, doi: 10.1520/F2792-12A.2.

[46] Y. Huang, M. C. Leu, J. Mazumder, and A. Donmez, "Additive manufacturing: Current state, future potential, gaps and needs, and recommendations," *J. Manuf. Sci. Eng. Trans. ASME*, vol. 137, no. 1, 2015, doi: 10.1115/1.4028725.

[47] Z. Xiang, M. Yin, Z. Deng, X. Mei, and G. Yin, "Simulation of forming process of powder bed for additive manufacturing," *J. Manuf. Sci. Eng. Trans. ASME*, vol. 138, no. 8, Aug. 2016, doi: 10.1115/1.4032970.

[48] T. Abu-Lebdeh, R. Damptey, V. Lamberti, and S. Hamoush, "Powder Packing Density and Its Impact on SLM-Based Additive Manufacturing," in *Minerals, Metals and Materials Series*, 2019, pp. 355–367, doi: 10.1007/978-3-030-05861-6_33.

[49] S. Pal *et al.*, "The effects of locations on the build tray on the quality of specimens in powder bed additive manufacturing," *Int. J. Adv. Manuf. Technol.*, vol. 112, no. 3–4, pp. 1159–1170, Jan. 2021, doi: 10.1007/s00170-020-06563-5.



https://doi.org/10.1016/j.rinma.2022.100264

[50] Q. B. Nguyen, D. N. Luu, S. M. L. Nai, Z. Zhu, Z. Chen, and J. Wei, "The role of powder layer thickness on the quality of SLM printed parts," *Arch. Civ. Mech. Eng.*, vol. 18, no. 3, pp. 948–955, 2018, doi: 10.1016/j.acme.2018.01.015.

[51] B. C. Salzbrenner *et al.*, "High-throughput stochastic tensile performance of additively manufactured stainless steel," *J. Mater. Process. Technol.*, vol. 241, pp. 1–12, 2017, doi: 10.1016/j.jmatprotec.2016.10.023.

[52] E. Louvis, P. Fox, and C. J. Sutcliffe, "Selective laser melting of aluminium components," *J. Mater. Process. Technol.*, vol. 211, no. 2, pp. 275–284, 2011, doi: 10.1016/j.jmatprotec.2010.09.019.

[53] M. A. Obeidi, E. McCarthy, L. Kailas, and D. Brabazon, "Laser surface texturing of stainless steel 316L cylindrical pins for interference fit applications," *J. Mater. Process. Technol.*, vol. 252, pp. 58–68, Feb. 2018, doi: 10.1016/J.JMATPROTEC.2017.09.016.

[54] H. Sohrabpoor, R. T. Mousavian, M. Obeidi, I. U. Ahad, and D. Brabazon, "Improving precision in the prediction of laser texturing and surface interference of 316L assessed by neural network and adaptive neuro-fuzzy inference models," *Int. J. Adv. Manuf. Technol.*, Aug. 2019, doi: 10.1007/s00170-019-04291-z.

[55] M. A. Obeidi, and B. Eng, "Laser processing of metallic surfaces for controlled micro-texturing and metallic bonding," 2018. Accessed: Jun. 24, 2021. [Online]. Available: http://doras.dcu.ie/22172/.

[56] M. Ghayoor, K. Lee, Y. He, C. hung Chang, B. K. Paul, and S. Pasebani, "Selective laser melting of 304L stainless steel: Role of volumetric energy density on the microstructure, texture and mechanical properties," *Addit. Manuf.*, vol. 32, 2020, doi: 10.1016/j.addma.2019.101011.

[57] D. Herzog, V. Seyda, E. Wycisk, and C. Emmelmann, "Additive manufacturing of metals," *Acta Mater.*, vol. 117, pp. 371–392, Sep. 2016, doi: 10.1016/j.actamat.2016.07.019.

[58] Q. B. Nguyen, Z. Zhu, F. L. Ng, B. W. Chua, S. M. L. Nai, and J. Wei, "High mechanical strengths and ductility of stainless steel 304L fabricated using selective laser melting," *J. Mater. Sci. Technol.*, vol. 35, no. 2, pp. 388–394, 2019, doi: 10.1016/j.jmst.2018.10.013.

[59] M. Ahmed Obeidi, E. McCarthy, S. I. Ubani, I. Ul Ahad, and D. Brabazon, "Effect of Surface Roughness on $CO_2$ Laser Absorption by 316L Stainless Steel and Aluminum," *Mater. Perform. Charact.*, vol. 8, no. 6, p. 20180091, Jun. 2019, doi: 10.1520/MPC20180091.

[60] A. El Hassanin, M. A. Obeidi, F. Scherillo, and D. Brabazon, "$CO_2$ laser polishing of laser-powder bed fusion produced AlSi10Mg parts," *Surf. Coatings Technol.*, vol. 419, p. 127291, 2021, doi: 10.1016/j.surfcoat.2021.127291.



https://doi.org/10.1016/j.rinma.2022.100264